*J. Fluid Mech.* (1983), *vol.*128, *pp.* 469–487
*Printed in Great Britain*



# Steady shallow flow over curved beds

By N. S. SIVAKUMARAN, T. TINGSANCHALI AND R. J. HOSKING†
Asian Institute of Technology, Bangkok, Thailand

(Received 29 September 1981 and in revised form 12 May 1982)

The validity of recent shallow-flow equations with bed curvature is examined. Subcritical, critical and supercritical steady-flow solutions are identified, and the point of critical flow on the bed located, in terms of a generalized Froude number. Experiments on steady flow over both a symmetric and unsymmetric bed profile show that the theory satisfactorily predicts the free-surface and bed-pressure profiles over $-2 \lesssim \kappa h \leqslant 0{\cdot}54$ (where $\kappa$ is the bed curvature and $h$ is the flow depth normal to the bed).

## 1. Introduction

Approximate nonlinear equations for shallow flow, generalizing the well-known Saint-Venant equations to account for one-dimensional bed curvature, have been derived by Dressler (1978) using an asymptotic approach. We re-derived these equations more simply, and applied them to steady shallow flow over a high overflow spillway crest and a spillway toe (cf. Sivakumaran, Hosking & Tingsanchali 1981). Comparison with experiments by the U.S. Army Engineers Waterways Experiment Station on a spillway crest (with vertical upstream face, without piers; cf. Chow 1959) demonstrated that the equations may be valid for quite large negative curvature (convex bed); but comparison with Henderson & Tierney's (1963) data on a spillway toe shows that they are limited to smaller positive curvature (concave bed). In §2 the theoretical validity of the shallow-flow equations is discussed in terms of a generalized Froude number. In §3 steady-flow solutions of the shallow-flow equations are considered; subcritical, critical and supercritical solutions exist and the location of the critical flow is identified. Experimental verification of the shallow-flow equations for steady flow over both a symmetric and unsymmetric bed profile is described in §4. The theoretical and experimental results are compared in §5.

## 2. Shallow-flow equations with bed curvature

Shallow flow over a curved bed is illustrated in figure 1. The flow depth $h(s,t)$ normal to the bed and the flow velocity $u_0(s,t)$ at the bed may be estimated from the shallow-flow equations (Dressler 1978; Sivakumaran *et al.* 1981):

$$(1-\kappa h)\frac{\partial h}{\partial t}+\frac{\partial q}{\partial s}=0, \quad \frac{1}{g}\frac{\partial u_0}{\partial t}+\frac{\partial E}{\partial s}=0, \tag{2.1), (2.2}$$

† Permanent address: University of Waikato, Hamilton, New Zealand.

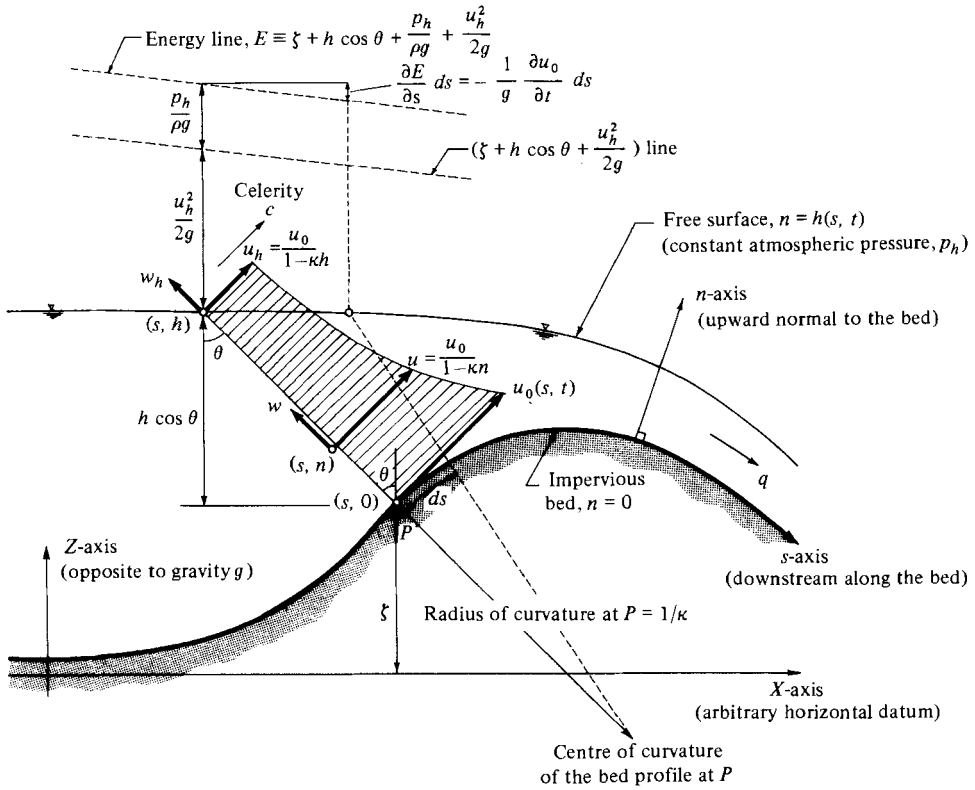


FIGURE 1. Definition sketch.

where the flow per unit width $q$ and energy head $E$ are

$$q(s,t) \equiv -\frac{u_0}{\kappa}\ln(1-\kappa h), \tag{2.3}$$

$$E(s,t) \equiv \zeta + h\cos\theta + \frac{p_h}{\rho g} + \frac{u_0^2}{2g}(1-\kappa h)^{-2}; \tag{2.4}$$

and the velocity components and pressure are given by

$$u(s,n,t) = \frac{u_0}{1-\kappa n}, \tag{2.5}$$

$$w(s,n,t) = \left[\frac{\ln(1-\kappa n)}{(1-\kappa n)\kappa}\right]\frac{\partial u_0}{\partial s} - \frac{1}{\kappa^2}\frac{d\kappa}{ds}\left[\frac{\kappa n}{(1-\kappa n)^2} + \frac{\ln(1-\kappa n)}{1-\kappa n}\right]u_0, \tag{2.6}$$

$$p(s,n,t) = p_h + \rho g(h-n)\cos\theta + \tfrac{1}{2}\rho u_0^2[(1-\kappa h)^{-2} - (1-\kappa n)^{-2}]. \tag{2.7}$$

All other notation is the same as in Sivakumaran *et al.* (1981), viz $\kappa$ is the curvature of the bed, $g$ the constant acceleration due to gravity, $s$ and $n$ the respective coordinates along and normal to the bed, and $t$ the time; the height $\zeta$ above some datum defines the bed profile, the angle $\theta$ measures bed slope, $p_h$ is the constant atmospheric pressure (often set equal to zero), and $\rho$ is the fluid density.

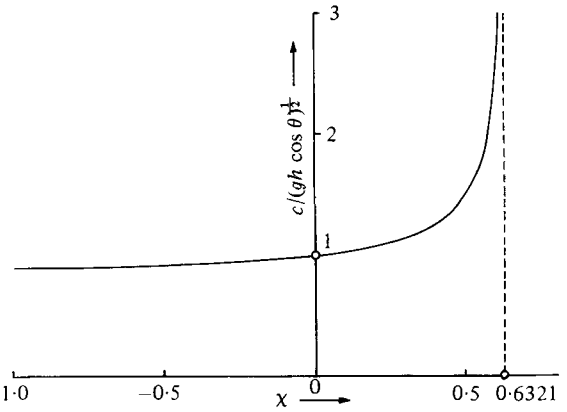


FIGURE 2. Relative celerity $c/(gh\cos\theta)^{\frac{1}{2}}$ versus dimensionless curvature $\chi$. (The curve is imaginary for $\chi > 0{\cdot}6321$ and has minimum 0·8776 at $\chi = -5{\cdot}0091$.)

For critical flow defined by $ds/dt = 0$, from the characteristics of (2.1) and (2.2) we have

$$\frac{u_0^2}{gh\cos\theta} = -\frac{(1-\chi)^3\ln(1-\chi)}{\chi[1+\ln(1-\chi)]}, \tag{2.8}$$

where $\chi \equiv \kappa h$. Dressler (1978) defined the left-hand side as the *local Froude number* $\mathscr{F}$, and identified the right-hand side as the *local critical Froude number* $\mathscr{F}_c$.

Equation (2.8) can be rewritten in terms of the free surface velocity component $u(s,h,t) \equiv u_h$ (cf. (2.5)) as

$$|u_h| = c, \tag{2.9}$$

where

$$c \equiv \left[-\frac{(1-\chi)\ln(1-\chi)}{\chi[1+\ln(1-\chi)]}gh\cos\theta\right]^{\frac{1}{2}} \tag{2.10}$$

is the *celerity* (i.e. the speed of small disturbances at the free surface) *in curved bed flow* (cf. figure 1); as $\kappa \to 0$ (flat bed) the well-known result $c = (gh\cos\theta)^{\frac{1}{2}}$ is recovered (cf. Henderson 1966). Thus at critical flow any small disturbance at the free surface travels with the same fluid particles. One may preserve the definition of Froude number originally introduced for flow over flat beds ($\kappa = 0$, cf. Henderson 1966), viz the ratio of free-surface speed to celerity

$$\mathbb{F} \equiv |u_h|/c, \tag{2.11}$$

which is 1 for critical flow, irrespective of bed curvature (cf. (2.9)). We recall that the flow is subcritical if $\mathbb{F} < 1$, and supercritical if $\mathbb{F} > 1$. From (2.8) we note that

$$\mathbb{F} = (\mathscr{F}/\mathscr{F}_c)^{\frac{1}{2}}. \tag{2.12}$$

The celerity (2.10) is singular where $1+\ln(1-\chi) = 0$ or $\chi = 1-e^{-1} \approx 0{\cdot}6321$, which defines an absolute upper bound for validity of the shallow-flow equations. Dressler (1978) suggested the upper bound $\chi_u = 0{\cdot}5$, and the lower bound $\chi_\ell = -0{\cdot}85$, where the critical-Froude-number curve and the local-Froude-number curve for bed pressure below atmospheric intersect. Within $(\chi_\ell, \chi_u)$ any small disturbance at the free surface spreads faster over a concave bed ($\kappa > 0$) but slower over a convex bed ($\kappa < 0$) than over a flat bed ($\kappa = 0$) (cf. figure 2).

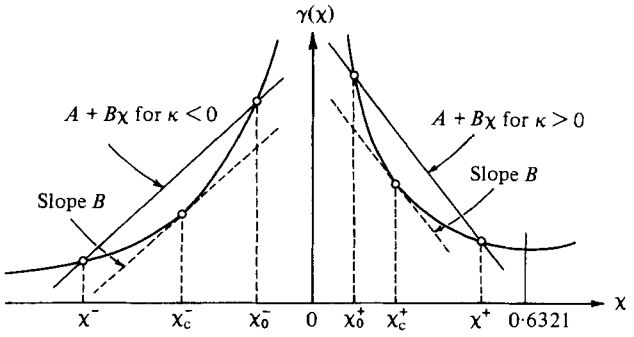


FIGURE 3. Solution of $\gamma(\chi) = A + B\chi$: $\chi^{\pm}$, subcritical; $\chi_c^{\pm}$, critical; $\chi_0^{\pm}$, supercritical.

## 3. Steady-flow solutions

The basic steady-flow equation (cf. Sivakumaran *et al.* 1981, equation (3.3)) is

$$E = \zeta + h\cos\theta + \frac{q^2\kappa^2}{2g}[(1-\kappa h)\ln(1-\kappa h)]^{-2}; \tag{3.1}$$

which can be expressed when $\kappa \neq 0$ as

$$\gamma(\chi) = A + B\chi, \tag{3.1'}$$

where

$$A \equiv \frac{2g(E-\zeta)}{(q\kappa)^2}, \quad B \equiv -\frac{2g\cos\theta}{q^2\kappa^3}, \tag{3.2a,b}$$

$$\chi \equiv \kappa h, \quad \gamma(\chi) \equiv [(1-\chi)\ln(1-\chi)]^{-2}. \tag{3.2c,d}$$

The graphical solution of (3.1′) is sketched in figure 3. As proved in appendix A,

$$\mathbb{F} \lessgtr 1 \Leftrightarrow \left|\frac{d\gamma(\chi)}{d\chi}\right| \lessgtr |B|; \tag{3.3}$$

the critical flow normally occurs at the point $x$ defined by setting $\mathbb{F} = 1$ in

$$\frac{dE}{dx} = (1-\chi)\frac{d\zeta}{dx} + (1-\mathbb{F}^2)\frac{\cos\theta}{\kappa}\frac{d\chi}{dx} + \frac{q^2\kappa}{2g}(2A+3B\chi)\frac{d\kappa}{dx} = 0. \tag{3.4}$$

(Equation (3.4) is obtained by differentiating the basic steady-flow equation (3.1) with respect to $x$.) For symmetric bed profiles $d\zeta/dx = d\kappa/dx = 0$ at the point of symmetry, so that (3.4) is trivially satisfied – i.e. critical flow occurs at the point of symmetry of the bed profile; for non-symmetric convex profiles, the point of critical flow is displaced from the crest (see below). The pressure follows from (2.7), given the solution of (3.1′) for the free surface.

As described in §4, we find that free-surface and bed-pressure profiles predicted by these shallow-flow equations coincide closely with experiment for a wide range of bed curvature ($-2 \lesssim \chi \leqslant 0{\cdot}54$). At this point we can demonstrate that the familiar Saint-Venant equations (ignoring curvature) predict significantly different free-surface and bed-pressure profiles over this range. If $h$ is the flow depth deduced from (3.1), and if we denote the depth predicted from Saint-Venant theory by $h(1+\epsilon_h)$, then the zero-curvature equation replacing (3.1) is

$$E = \zeta + h(1+\epsilon_h)\cos\theta + \frac{q^2}{2gh^2}(1+\epsilon_h)^{-2}.$$

Subtracting, we have that the dimensionless deviation $\epsilon_h$ satisfies the cubic

$$\epsilon_h^3 + (2-\alpha)\,\epsilon_h^2 + (1-2\alpha)\,\epsilon_h + \beta - \alpha = 0, \tag{3.5}$$

where $$\alpha \equiv -\frac{(1-\chi)\ln(1-\chi)}{2\chi[1+\ln(1-\chi)]}\mathbb{F}^2, \quad \beta \equiv \left[-\frac{(1-\chi)\ln(1-\chi)}{\chi}\right]^2\alpha;$$

for typical values of the Froude number the magnitude of the root passing through the origin for zero curvature ($\chi = 0$) becomes $O(1)$ at quite-moderate curvature ($|\chi| \lesssim 0{\cdot}5$). The error in predicting the bed-pressure profile is also significant: in this case the Saint-Venant (hydrostatic) equation is $p_0 = \rho g h(1+\epsilon_h)\cos\theta$, so that subtracting from (2.7) for $n = 0$ we have the deviation

$$\epsilon_p \equiv \frac{\Delta p_0}{\rho g h \cos\theta} = \epsilon_h + \mathbb{F}^2\,\Omega(\chi), \tag{3.6}$$

where $\Omega(\chi) \equiv (1-\frac{1}{2}\chi)(1-\chi)\ln(1-\chi)[1+\ln(1-\chi)]^{-1}$ is also $O(1)$ for $|\chi| \lesssim 0{\cdot}5$.

## 4. Experimental set-up

The experiments to test the equations were carried out in a 915 × 75 × 44·5 cm flume made of a steel frame with glass windows on both vertical sides (cf. figure 4). The bed of 1·5 cm thick plywood was elevated 10 cm above the base of the flume, to house the plastic tubes connecting the piezometer tappings along the centreline of the curved-bed model and the piezometers. The flume width was vertically partitioned along the entire channel length into two compartments, again using 1·5 cm plywood. The larger compartment was 30 cm wide, and served as the test channel for steady flow over two curved-bed models (see below). The bed-pressure piezometers were set up within the smaller compartment. The inflow to the inlet box through a 15·24 cm diameter cast-iron pipe was controlled by a gate valve.

A 7·6 cm diameter orifice, placed well before the control valve in the inlet pipe, rated the inflow. Because of rapid oscillation of the mercury column in the U-tube manometer attached to both sides of this orifice, about 25 readings of the simultaneous mercury levels in both legs of the manometer were recorded at about 10 s intervals to estimate the mercury-level difference $H$ (cm).† The accuracy of the manometer scale was 0·1 cm. From the orifice equation (cf. Streeter & Wylie 1975), the steady unit-width discharge $q = 157{\cdot}03H^{\frac{1}{2}}$ cm$^3$ s$^{-1}$ cm$^{-1}$ (at 27 °C) was then determined.

A portable trolley carrying a point gauge of accuracy 0·01 cm was placed on two rails fixed along the flume top. At a flat-bed section of the channel (say the section 350 cm from the inlet box), the water depth $D$ (cm) was measured using this point gauge to give the energy head $E = D + q^2/2gD^2$ (cm). The point gauge was also used to measure the water depth at every 5 cm horizontal interval along the centreline of the curved-bed model. Although theory defines the free surface by the coordinate $n$ normal to the bed, we measured the vertical coordinate $z$ to locate the free surface. Vertical measurements are easier than measurements normal to the bed, which involve varying the inclination of the gauge from point to point; and we can readily compute the corresponding depths normal to the bed (cf. appendix B).

Along the centreline of the curved-bed model, 0·32 cm diameter copper piezometer tappings were fixed at 5 cm horizontal intervals; these were connected by long plastic

† Two small valves at either side of the orifice (one upstream and one downstream) were operated to remove trapped air in the pipeline, so that the amplitude of the oscillation was no more than 5% of the measured head.

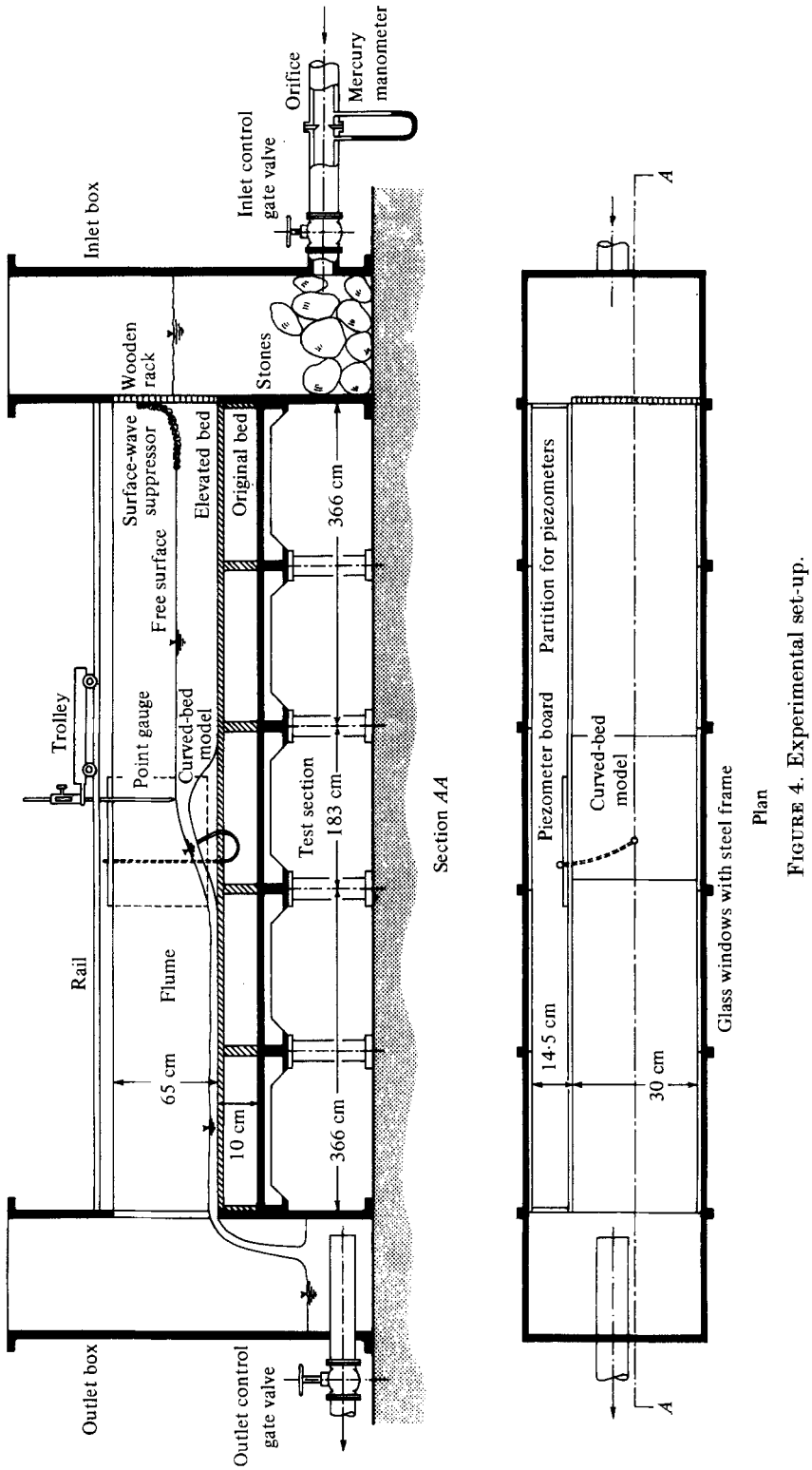


FIGURE 4. Experimental set-up.

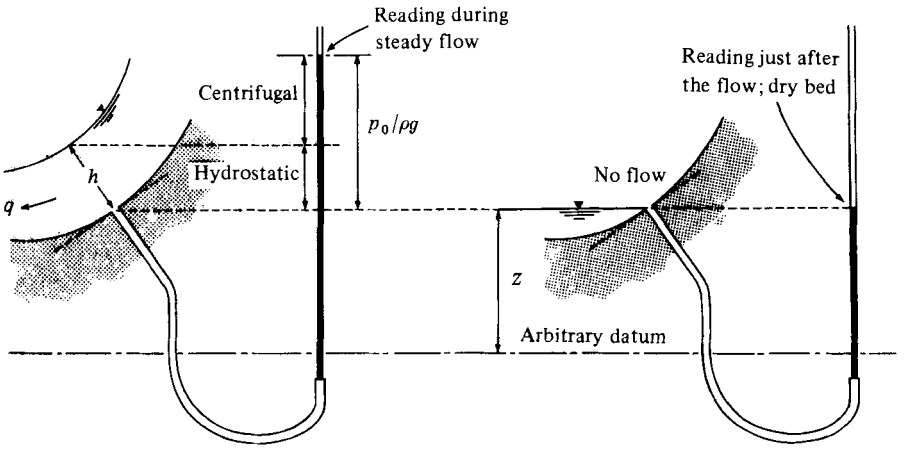


FIGURE 5. Reading the bed pressure.

tubes of 0·64 cm internal diameter to vertical water piezometers (0·64 cm external diameter glass tubes) of reading accuracy to 0·1 cm. As depicted in figure 5, the recorded piezometric level difference between the steady flow and the dry-bed condition† gave the gauge bed-pressure head $p_0/\rho g$, where the implicit pressure datum taken corresponds to $p_h = 0$.

The shallow-flow equations were examined for steady flow over two curved-bed models, one a *symmetric profile* shaped after the normal distribution and the other an *unsymmetric profile* fashioned by $B$-splines (cf. appendix C). The leading edge of each test section was placed 366 cm downstream from the inlet box.

Potassium permanganate solution was injected from an overhead container through a 0·15 cm diameter nozzle at different points in the flow field, to trace the flow pattern (cf. figure 6). The well-defined flow downstream is typical.

We can anticipate that turbulent boundary-layer development does not significantly alter the flow depth. Following Bauer (1954), we have

$$\frac{\delta}{s} = \frac{0{\cdot}024}{(s/k)^{0{\cdot}13}},$$

where $\delta$ is the boundary-layer thickness, $s$ is the distance from the crest along the bed in the flow direction, and $k$ is the roughness height. For our PVC curved-bed models, we have $k \approx 0{\cdot}2$ mm, corresponding to the Manning roughness coefficient $n = 0{\cdot}01$ (cf. Henderson 1966, pp. 98, 99). If we also estimate that the boundary layer increases the flow depth by displacement thickness $0{\cdot}1\delta$ this is no more than a few per cent. In passing we note that $k \approx 0{\cdot}6$–$1{\cdot}5$ mm, corresponding to Manning roughness coefficient $n = 0{\cdot}012$–$0{\cdot}014$ for a concrete surface of a prototype dam spillway. In this case the boundary-layer thickness could be up to 30% greater; but of course the flow depth may be very much deeper, so that the effect would be less significant.

† The procedure followed to get the 'dry-bed' reading was to close the flume valves and add water to the level of the model crest, then remove any trapped air in each manometer, before slowly draining to a level just covering each manometer opening in turn.

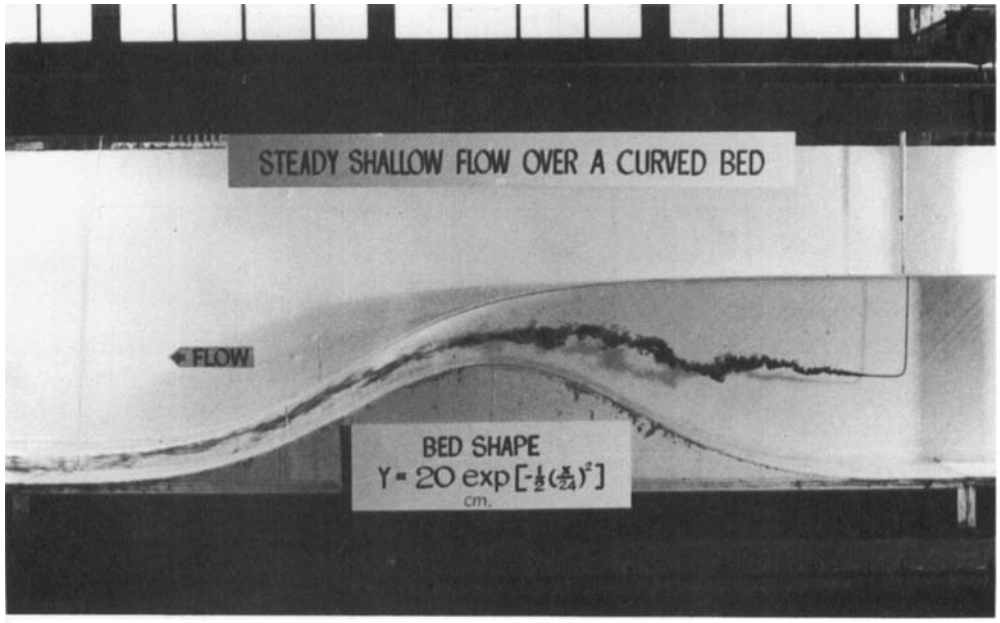


(*a*)

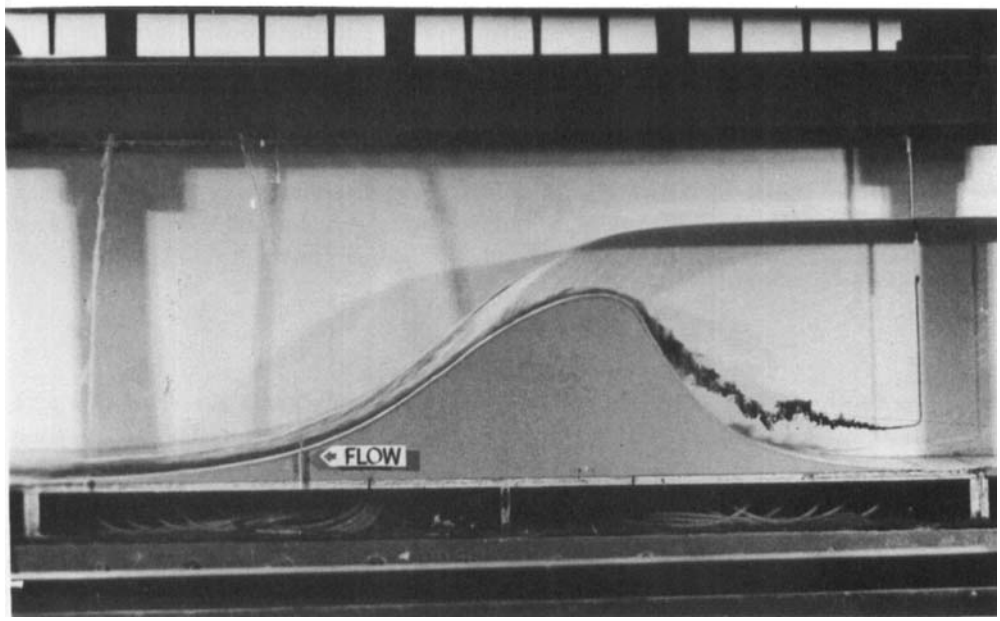


(*b*)

FIGURE 6. (*a*) Steady flow over the symmetric profile for $q = 1119{\cdot}7$ cm$^3$ s$^{-1}$ cm$^{-1}$ and $E = 34{\cdot}8$ cm. (*b*) Steady flow over the unsymmetric profile for $q = 1116{\cdot}5$ cm$^3$ s$^{-1}$ cm$^{-1}$ and $E = 44{\cdot}7$ cm.

## 5. Results

Figures 7 (*a*, *b*) show experimental points and theoretical curves for the free surface and bed pressure for flow over the *symmetric* profile, for a high and a low flow respectively. (Similar curves were obtained for other intermediate flows – cf. Sivakumaran (1981)). Note that the complete theoretical bed-pressure profiles are symmetric about the crest point $x = 0$; as appropriate, subcritical and supercritical pressure profiles are selected for upstream and downstream respectively. Agreement is excellent, although for larger $q$ the theoretical free surface is slightly below the experimental points in the subcritical region; the inadequacy of the shallow-flow approximation where the flow is deep probably accounts for this. Critical flow occurs exactly at the crest, as predicted by (3.4) – see also figure 8, which is primarily intended to show the close agreement between theoretical and observed local Froude number (cf. also Dressler 1978). Near the crest in the subcritical region the experimental

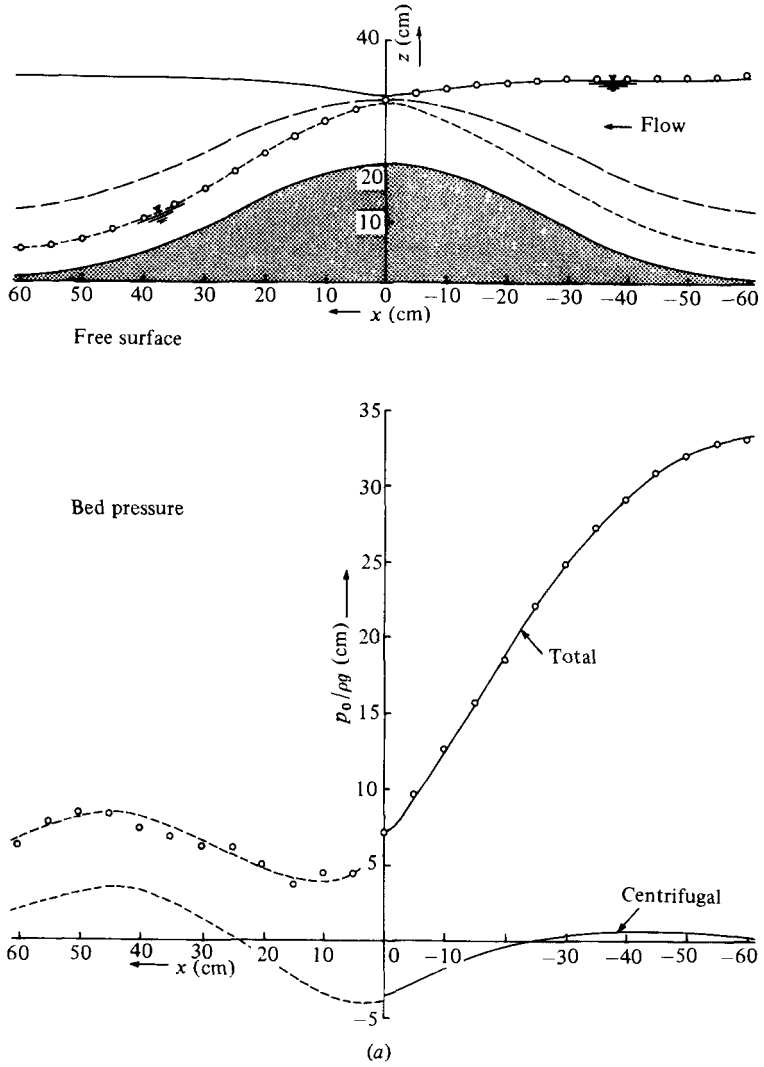


(*a*)

FIGURE 7 (*a*). For caption see p. 468.

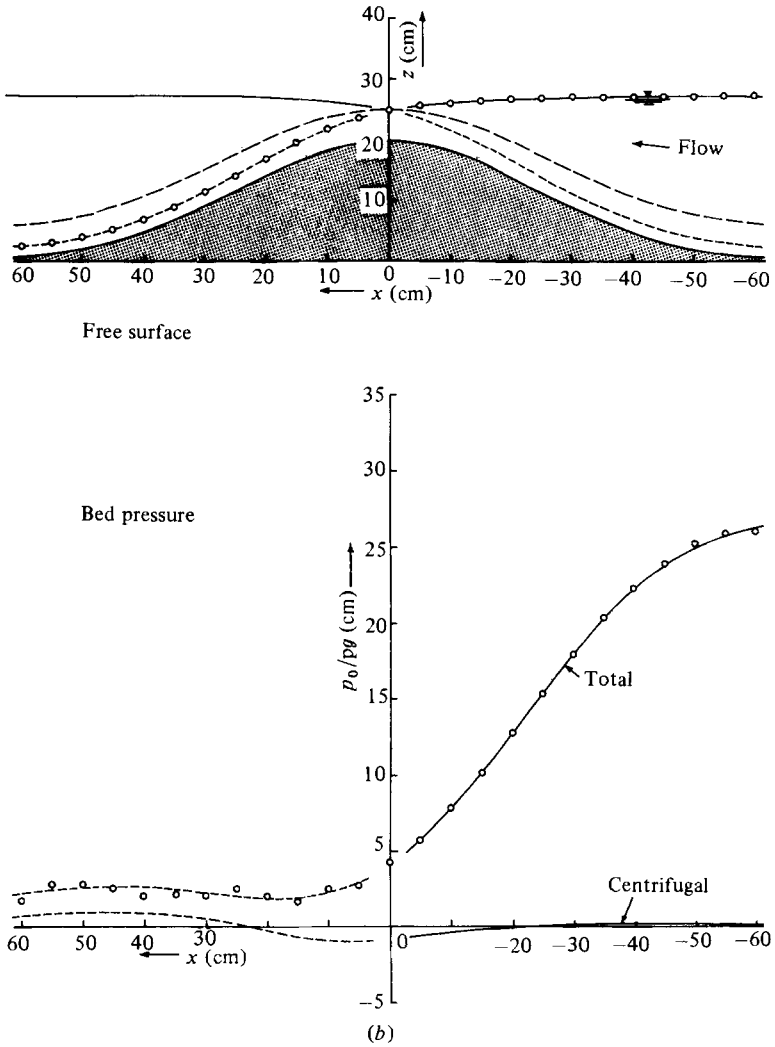


FIGURE 7. (*a*) Steady flow over the symmetric profile for $q = 1119{\cdot}7$ cm$^3$ s$^{-1}$ cm$^{-1}$ and $E = 34{\cdot}8$ cm (highflow). (*b*) Steady flow over the symmetric profile for $q = 359{\cdot}9$ cm$^3$ s$^{-1}$ cm$^{-1}$ and $E = 27{\cdot}2$ cm (lowflow). Theory: ——, subcritical; – – –, critical; ----, supercritical. Experiment: ○.

points fall below the theoretical free surface of subcritical flow as the flow accelerates in a *transition region* from sub- to supercritical flow. For low flow, no solution of (3.1′) exists near the *transition point* – cf. the discontinuity at the crest in figure 7(*b*).

The large change of velocity gradient in the transition region implies that the basic assumptions of the approximate shallow-flow equations examined (viz *grossly irrotational inviscid flow*) are questionable there. However, we may continue to characterize the transition by rewriting (3.4) as

$$\frac{d\chi}{d\theta} = \frac{-(1-\chi)\sin\theta - \dfrac{q^2\kappa^2}{2g}(2A+3B\chi)\dfrac{d\kappa}{d\theta}}{(1-F^2)\cos\theta} \equiv \frac{\Phi(\theta,\chi)}{\Psi(\theta,\chi)},$$

and noting that we are interested in the neighbourhood of the singular point where $\Phi = \Psi = 0$, viz $(\theta_0 \approx 0, \chi_0)$ when $d\kappa/d\theta \approx 0$. For small curvature variation the nature

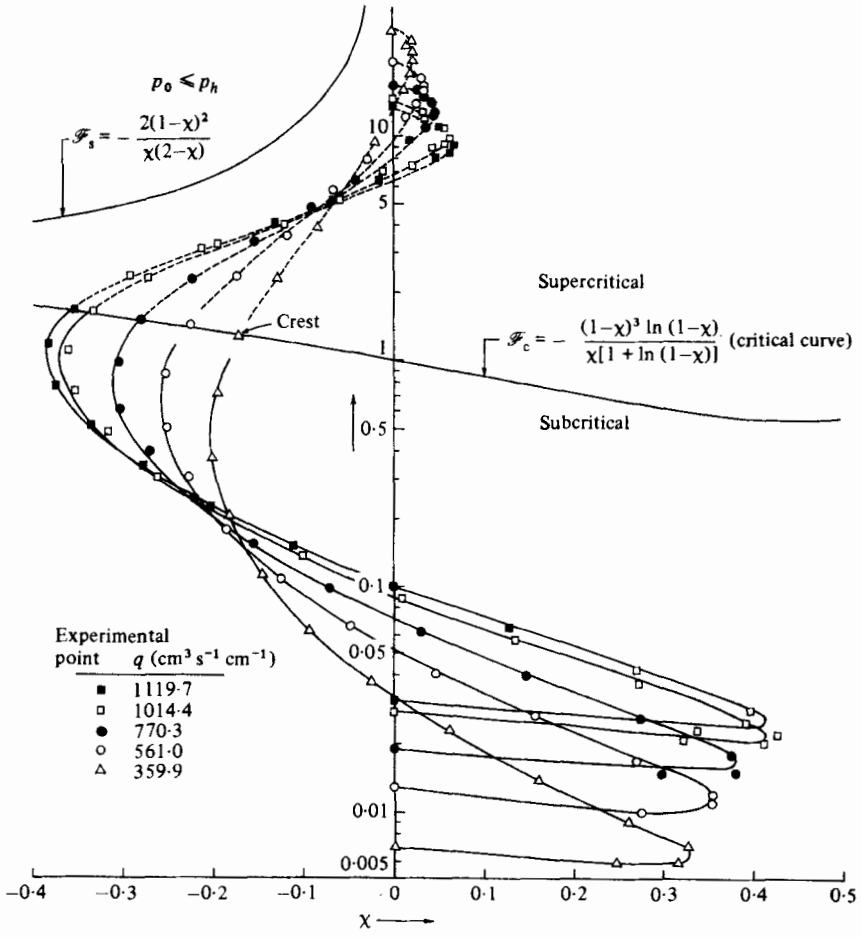


FIGURE 8. Theoretical and experimental local Froude number versus dimensionless curvature for the symmetric profile.

of the transition profile can therefore be inferred from the linearized autonomous system (cf. also the transition-profile discussion of Escoffier 1958; Chow 1959):

$$\frac{d\chi}{d\lambda} = -(1-\chi_0)\,\theta,$$

$$\frac{d\theta}{d\lambda} = \frac{q^2\kappa^3}{g} m^2(1-\chi_0)\,(\chi-\chi_0),$$

where the function $$m^2(1-\chi_0) = 3\frac{[\ln(1-\chi_0)+\frac{5}{6}]^2+\frac{11}{36}}{[(1-\chi_0)\ln(1-\chi_0)]^4} > 0.$$

The corresponding integral curves are

$$\theta^2 + \frac{q^2\kappa^3}{g} m^2(\chi-\chi_0)^2 = \text{constant},$$

i.e. hyperbolae for a convex bed ($\kappa < 0$), defining a saddle. Owing to dissipation ($dE/ds \neq 0$), the actual surface profile departs from its upstream ideal integral curve, to pass through the critical point before merging with its downstream curve opposite.

| $q$ | $E$ | $\chi_{min}$ | | | $\chi_{max}$ | | |
|---|---|---|---|---|---|---|---|
| ($cm^3\ s^{-1}\ cm^{-1}$) | (cm) | Experiment | Theory | $x$ (cm) | Experiment | Theory | $x$ (cm) |
| 1119·7 | 34·8 | −0·380 | −0·385 | −5 | 0·427 | 0·417 | −55 |
| 1014·4 | 34·0 | −0·360 | −0·370 | −5 | 0·413 | 0·407 | −55 |
| 770·3 | 31·7 | −0·304 | −0·310 | −5 | 0·381 | 0·377 | −55 |
| 561·0 | 29·6 | −0·253 | −0·256 | −10 | 0·355 | 0·352 | −50 |
| 359·9 | 27·2 | −0·201 | −0·201 | −10 | 0·328 | 0·326 | −50 |

TABLE 1. Extreme $\chi$-values and their location (symmetric profile)

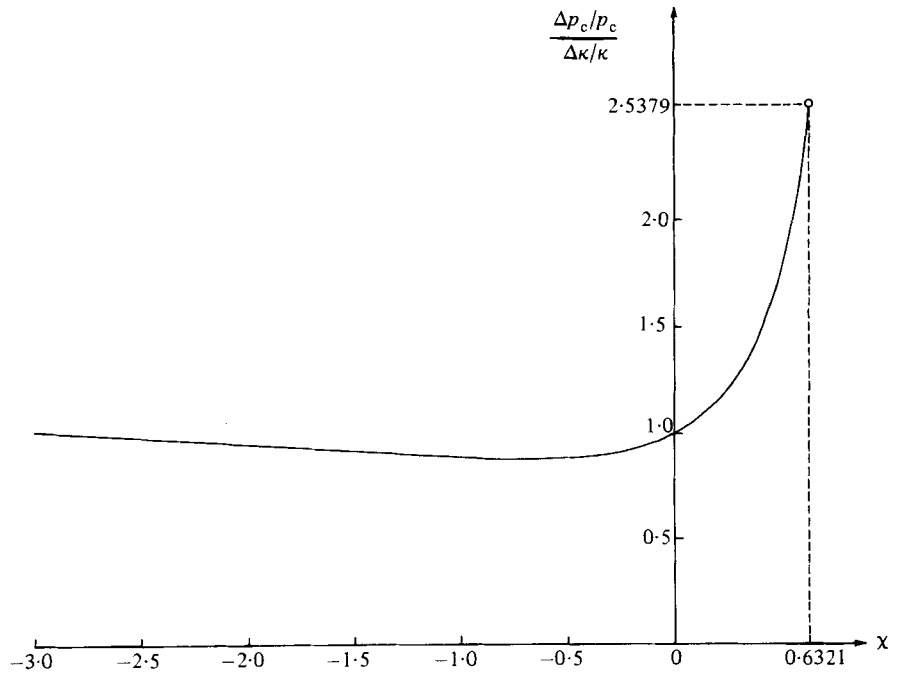


FIGURE 9. Variation of error ratio $(\Delta p_c/p_c)/(\Delta\kappa/\kappa)$ versus $\chi$ (the uncertainty relation (5.3)).

The integral curve for the high flow in figure 7 (*a*) is shown entirely; but for the low flow of figure 7 (*b*), in the neighbourhood of the singular point, it is a hyperbola *cutting* the critical curve, and we have chosen not to continue through the cut.

Table 1 summarizes extreme $\chi$-values and their location, for flows (various $q$ and $E$) for which the symmetric profile was tested; and *all* values fall *within* the range suggested by Dressler (1978):

$$-0{\cdot}85 \leqslant \kappa h \leqslant 0{\cdot}5. \tag{5.1}$$

The total bed pressure is accurately predicted, particularly upstream where the centrifugal pressure is small. It is clear that measuring bed pressure $p_0$ disturbs the bed curvature. We can show from (2.7) on eliminating $u_0$ using (2.3) that the centrifugal bed pressure

$$p_c = \frac{\rho q^2}{2h^2}\Lambda(\chi), \quad \Lambda(\chi) \equiv \chi^3(2-\chi)\gamma(\chi) \tag{5.2}$$

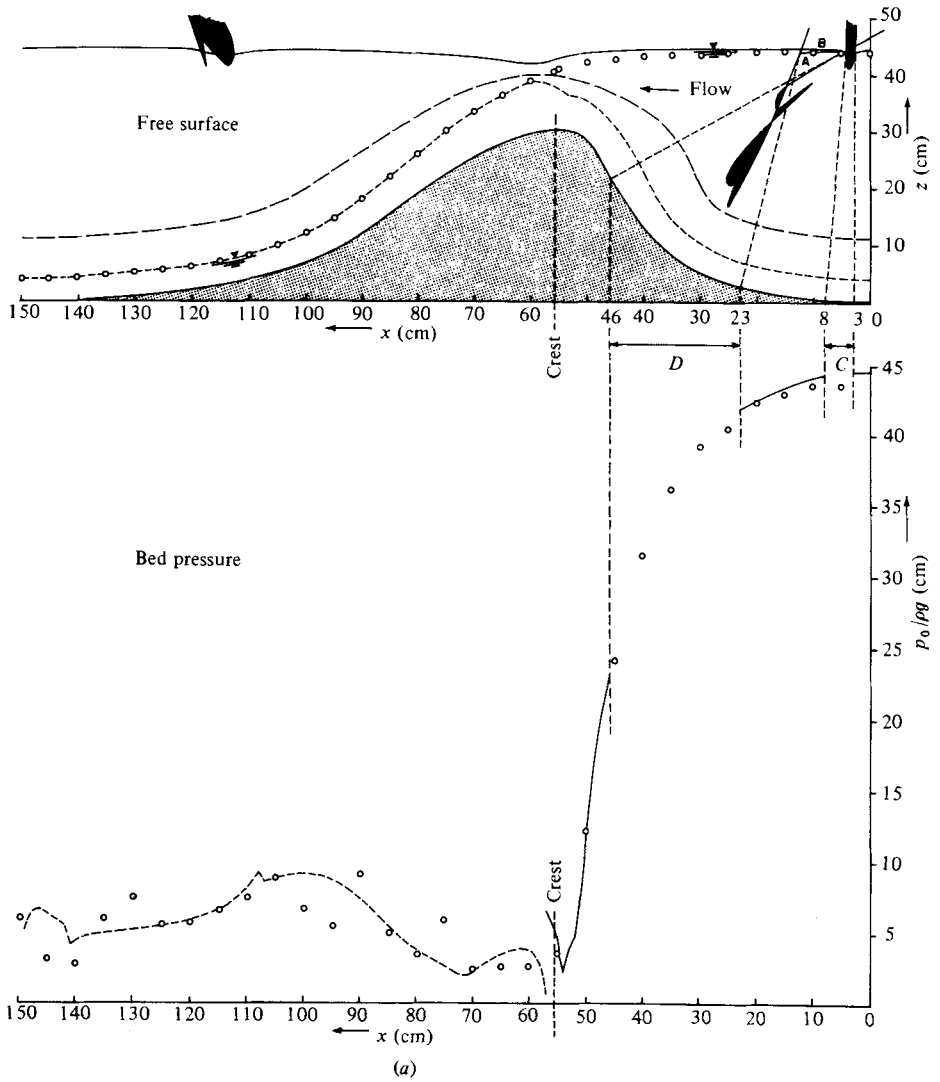


FIGURE 10(*a*). For caption see p. 482.

can be affected by bed curvature error. Considering the logarithmic partial differentiation of (5.2) with respect to $\kappa$, we get the error ratio

$$\frac{\Delta p_c/p_c}{\Delta\kappa/\kappa} = \frac{d\Lambda/d\chi}{\Lambda}\chi = \frac{2[(\chi^2-3\chi+3)\ln(1-\chi)+2\chi-\chi^2]}{(2-\chi)(1-\chi)\ln(1-\chi)}, \tag{5.3}$$

where $\Delta p_c$ is the error (uncertainty) in the measured centrifugal pressure due to an error (uncertainty) $\Delta\kappa$ in the bed curvature (cf. figure 9). Local curvature error and resulting turbulence (e.g. due to the flat-end piezometer tappings) may account for the systematic error pattern in the measured bed-pressure profiles in the downstream supercritical region (cf. also the discussion below).

In the symmetric profile, the experimental $\chi$-values fell within the range suggested by Dressler – i.e. (5.1). To test the validity of this range an *unsymmetric* bed profile, skewed upstream, was designed using a $B$-splined shape (cf. appendix C). Figures

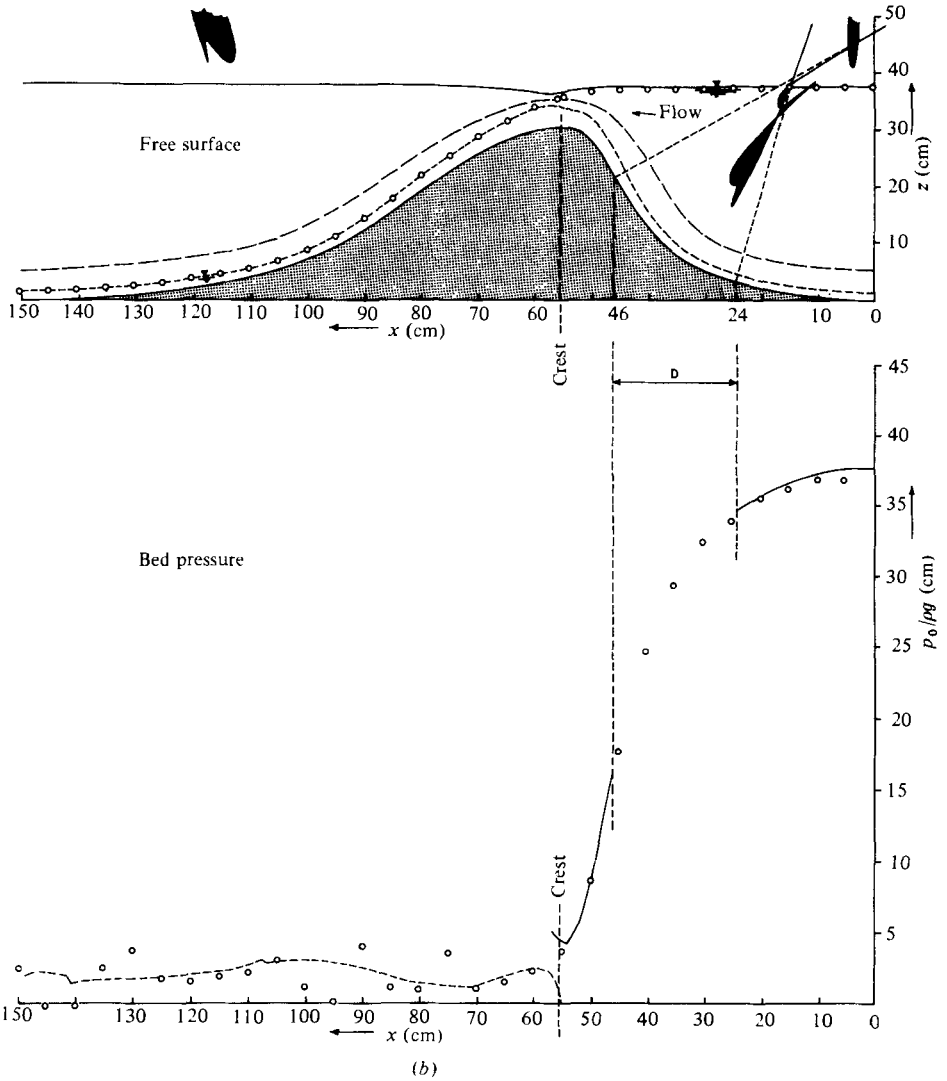


FIGURE 10. (*a*) Steady flow over the unsymmetric profile for $q = 1116{\cdot}5$ cm$^3$ s$^{-1}$ cm$^{-1}$ and $E = 44{\cdot}7$ cm (high flow). (*b*) Steady flow over the unsymmetric profile for $q = 375{\cdot}0$ cm$^3$ s$^{-1}$ cm$^{-1}$ and $E = 37{\cdot}8$ cm (low flow). Theory: ——, subcritical; – – –, critical; - - - -, supercritical. Experiment ○, ■, domains where $n \geqslant 0{\cdot}6321/\kappa$. *C*, *D*, intervals where bed pressure cannot be predicted.

| $q$ | $E$ | $\chi_{\min}$ | | | $\chi_{\max}$ | | |
|---|---|---|---|---|---|---|---|
| (cm$^3$ s$^{-1}$ cm$^{-1}$) | (cm) | Experiment | Theory | $x$ (cm) | Experiment | Theory | $x$ (cm) |
| 1116·5 | 44·7 | −2·808 | −3·020 | 40 | 0·543 | 0·543 | 5 |
| 905·3 | 42·9 | −2·236 | −2·445 | 45 | 0·526 | 0·527 | 5 |
| 745·8 | 41·6 | −2·070 | −2·260 | 45 | 0·521 | 0·523 | 5 |
| 375·0 | 37·8 | −1·608 | −1·692 | 40 | 0·502 | 0·506 | 5 |

TABLE 2. Extreme $\chi$-values and their location (unsymmetric profile)

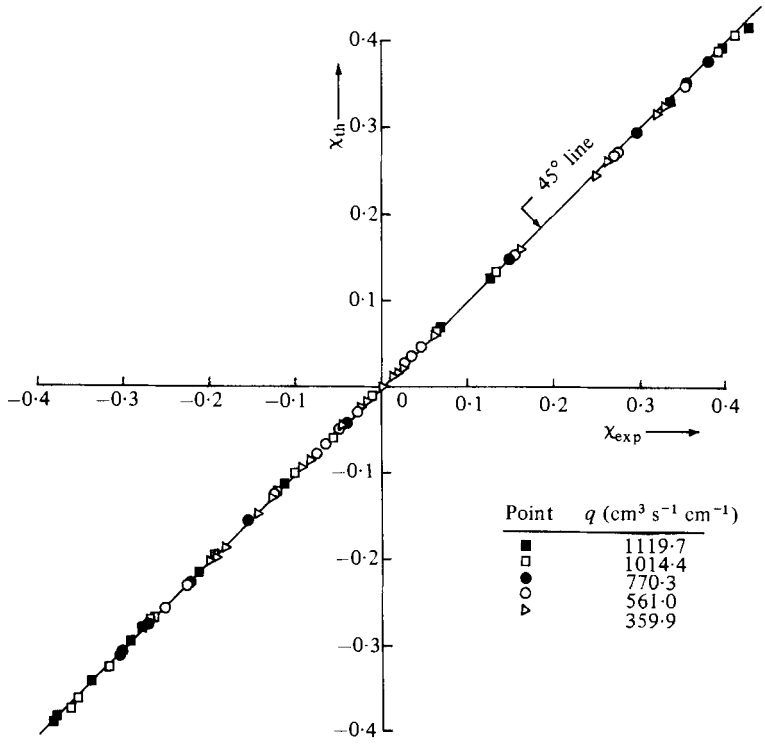


FIGURE 11. Theoretical versus experimental $\chi$ for the symmetric profile. The error $\chi_{exp} - \chi_{th}$ has mean 0·0013 and standard deviation 0·0023.

10($a$, $b$) show the experimental and theoretical free surface and bed pressure for a high and low flow. (Similar curves were obtained for other intermediate flows – cf. Sivakumaran (1981).) Again, the theoretical bed-pressure profiles are not continued through the crest, and, as in the case of the symmetric profile, subcritical and supercritical pressure profiles are selected for upstream and downstream respectively. The transition zone in which the flow changes from sub- to supercritical is more extensive in this case, and apparently the critical flow does not occur at the crest but slightly downstream as expected (cf. (3.4)). Table 2 gives the extreme $\chi$-values and their location – note that in this case $x$ is measured from the leading edge of the profile. The extremes are *outside* Dressler's suggested range (5.1), especially for negative $\chi$.

Bed pressure cannot be predicted for certain $x$-intervals (e.g. intervals $C$ and $D$ for $q = 1116{\cdot}5$ cm$^3$ s$^{-1}$ cm$^{-1}$ (cf. figure 10$a$) because the $\chi$-values are outside the theoretical limit, viz $\chi = 0{\cdot}6321$. The shaded areas in figures 10($a$, $b$) indicate the domains where no theoretical solution exists. For larger $q$, the free-surface prediction is not unique for certain $x$ near the origin. For instance, when $q = 1116{\cdot}5$ cm$^3$ s$^{-1}$ cm$^{-1}$ (cf. figure 10$a$) the bed normals for $x$ between the intervals $C$ and $D$ give the free surface marked by $A$, and for $x$ beyond the interval $D$ they give $B$. Let us call this phenomenon *normal-crossing* – since it corresponds to bed normals crossing each other. If normal-crossing occurs within the flow then the bed normals between the respective crossing normals appear redundant for free-surface prediction but necessary for bed pressure. If the domain of no solution ($\chi \geqslant 0{\cdot}6321$) does not exist

within normal-crossing, then these bed normals give a third free-surface prediction! Dressler's (1978) non-zero-Jacobian condition at the free surface, i.e.

$$J_h\left(\frac{x,z}{s,n}\right) = 1-\chi > 0,$$

seems insufficient for *uniqueness* of the predicted free surface.

There is no continuous prediction of either free surface or bed pressure across the transition point (cf. figures 10*a*, *b*). Apart from curvature error introduced by the piezometer tappings, other model-fabrication curvature errors probably account for larger systematic errors in the observed bed pressure downstream (cf. also Sivakumaran *et al.* 1981). (Matched $B$-splines give a *class*-2 curve – i.e. *continuous together with its first two derivatives* – therefore $\kappa$ is continuous everywhere but $d\kappa/dx$ is not; the discontinuity in $d\kappa/dx$ causes *kinks* in the theoretical bed pressure.)

The theoretical $\chi \equiv \kappa h$ values are plotted against the experimental $\chi$-values in figures 11 and 12 for the symmetric and the unsymmetric profiles respectively. There is good agreement for $-2 \lesssim \kappa h \leqslant 0{\cdot}54$, *beyond* Dressler's recommended range of validity (5.1) for his equations.

## 6. Conclusions

The shallow-flow equations with bed curvature are easy to use to predict free surface and bed pressure (hydrostatic + centrifugal) satisfactorily for irrotational steady flow when frictional effects are negligible. The equations are valid for convex beds of larger curvature than is the case for concave beds; the range $-2 \lesssim \kappa h \leqslant 0{\cdot}54$ shows good agreement between theory and experiment (cf. Dressler's suggested range $-0{\cdot}85 \leqslant \kappa h \leqslant 0{\cdot}5$).

The location of the critical flow can be accurately predicted. In supercritical flow any error in the bed curvature affects the bed pressure considerably. Near the singular point (i.e. transition point), the basic assumptions of the approximate shallow-flow equations examined are questionable.

## Appendix A. Fundamental lemma

*Theorem:*

$$\mathscr{F} \lessgtr 1 \Leftrightarrow \left|\frac{d\gamma(\chi)}{d\chi}\right| \lessgtr |B|.$$

To prove this we recall Dressler's (1978) definitions of local Froude number $\mathscr{F}$ and local critical Froude number $\mathscr{F}_c$ (cf. (2.8)); using (2.3) to eliminate $u_0$

$$\mathscr{F} \lessgtr \mathscr{F}_c \Leftrightarrow \frac{[-\kappa q/\ln(1-\chi)]^2}{gh\cos\theta} \lessgtr -\frac{(1-\chi)^3\ln(1-\chi)}{\chi[1+\ln(1-\chi)]},$$

or

$$\frac{2g\cos\theta}{q^2\kappa^3}\chi \gtrless -\frac{2[1+\ln(1-\chi)]}{[(1-\chi)\ln(1-\chi)]^3}\chi.$$

Comparing with (3.2) and denoting $d/d\chi$ by a prime, we get

$$\mathscr{F} \lessgtr \mathscr{F}_c \Leftrightarrow -B\chi \gtrless -\gamma'(\chi)\chi.$$

Therefore when

$$\left.\begin{aligned} &\chi > 0 \quad \mathscr{F} \lessgtr \mathscr{F}_c \Leftrightarrow -B \gtrless -\gamma'(\chi), \\ &\chi < 0 \quad \mathscr{F} \gtrless \mathscr{F}_c \Leftrightarrow B \gtrless \gamma'(\chi) \end{aligned}\right\} \Leftrightarrow |B| \gtrless |\gamma'(\chi)|.$$

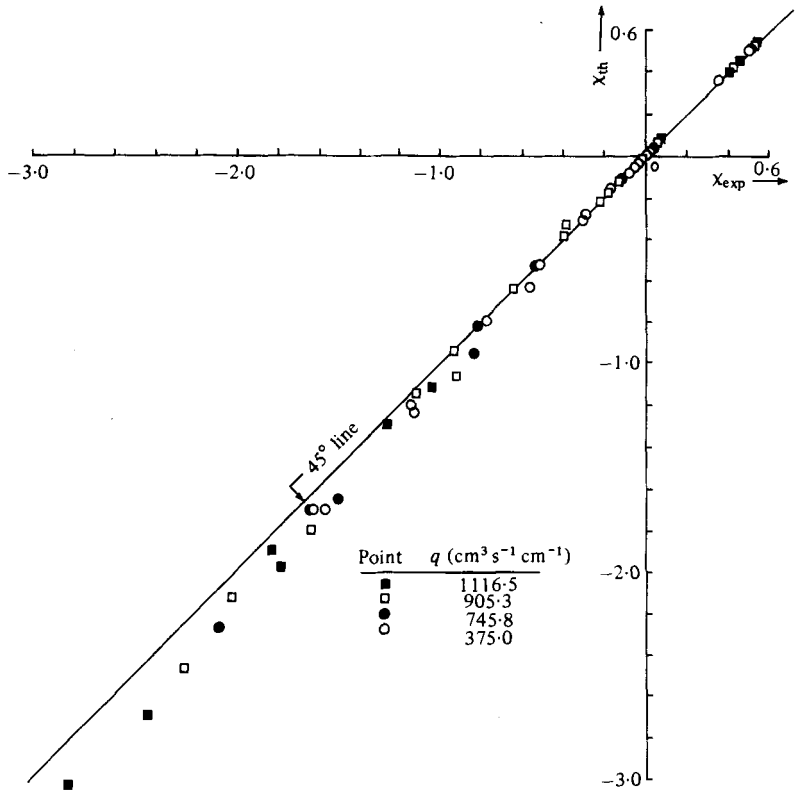


FIGURE 12. Theoretical versus experimental $\chi$ for the unsymmetric profile. The error $\chi_{exp}-\chi_{th}$ has mean 0·0265 and standard deviation 0·0599.

## Appendix B. Theoretical and experimental $\chi$

As shown in figure 13, at point $X_1$ the vertical depth $D_1$ on the point gauge gives the experimental free-surface coordinates $(X_1, Z_1 \equiv \zeta_1 + D_1)$,† and we compute the theoretical free-surface location $(x_1, z_1)$ on the same bed normal through $(X_1, Z_1)$ as follows.

Given the bed profile $\zeta(x)$, the solution of

$$\frac{\zeta(x)-Z_1}{x-X_1}\zeta'(x)+1=0 \tag{B 1}$$

(a prime denotes $d/dx$) is the base location $(x_2,\ \zeta_2 \equiv \zeta(x_2))$ of this bed normal, and at this point

$$\tan\theta_2 = \zeta'(x_2), \quad \kappa_2 = \zeta''(x_2)\cos^3\theta_2; \tag{B 2), (B 3}$$

the experimental flow depth and $\chi$ are given by

$$H_2 = [(X_1-x_2)^2+(Z_1-\zeta_2)^2]^{\frac{1}{2}}, \quad \chi_{exp} = \kappa_2 H_2. \tag{B 4), (B 5}$$

The theoretical $\chi$ is the solution of (3.1′); i.e.

$$\gamma(\chi) = A_2 + B_2\chi, \tag{B 6}$$

† Capital letters denote the experimental values, the lower-case letters the theoretical values.

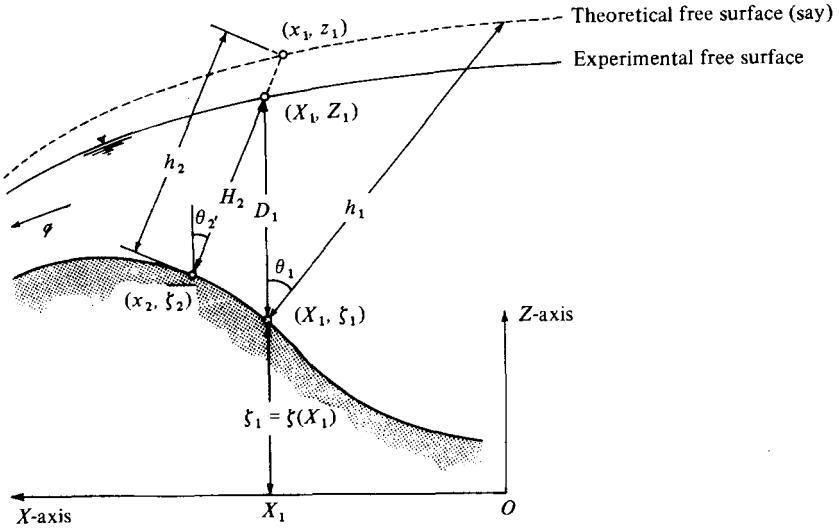


FIGURE 13. Theoretical and experimental flow depths.

where from (3.2) $A_2 \equiv 2g(E-\zeta_2)/(q\kappa_2)^2$ and $B_2 \equiv -2g\cos\theta_2/q^2\kappa_2^3$. The theoretical flow depth is

$$h_2 = \chi_{\text{th}}/\kappa_2; \tag{B 7}$$

hence the theoretical location of the free surface is given by

$$x_1 = x_2 - h_2\sin\theta_2, \quad z_1 = \zeta_2 + h_2\cos\theta_2. \tag{B 8}$$

Newton–Raphson iteration was used to solve (B 1) for the base location $(x_2, \zeta_2)$, and (B 6) for $\chi$.

## Appendix C. Geometry of curved-bed profiles

### (a) *Symmetric profile*

The symmetric profile of length 120 cm is described by the *normal distribution*

$$\zeta = 20\exp[-\tfrac{1}{2}(\tfrac{1}{24}x)^2] \quad \text{(cm)}. \tag{C 1}$$

### (b) *Unsymmetric profile*

The unsymmetric profile of length $L = 150$ cm is designed using $B$-splines (De Boor 1978; Loganantharaj 1981) as follows.

Let $I_i$ be $x$-intervals $X_i < x \leqslant X_{i+1}$, and let $V_i \equiv (X_i, Y_i)$ be vertices, where $i = 0, 1, \ldots, m-1$, $V_0 \equiv (0,0)$ and $V_m \equiv (L, 0)$. In terms of parameter $\lambda \in \{0, 1\}$ in $I_i$, a point $(\xi(\lambda), \zeta(\lambda))$ on the spline curve is given by

$$\eta(\lambda) = \tfrac{1}{6}(\lambda^3 \quad \lambda^2 \quad \lambda \quad 1)\begin{bmatrix} -1 & 3 & -3 & 1 \\ 3 & -6 & 3 & 0 \\ -3 & 0 & 3 & 0 \\ 1 & 4 & 1 & 0 \end{bmatrix}\begin{bmatrix} V_{i-1} \\ V_i \\ V_{i+1} \\ V_{i+2} \end{bmatrix} \text{(cm)}, \tag{C 2}$$

where $\eta \leftarrow \xi$ when $V \leftarrow X$, and $\eta \leftarrow \zeta$ when $V \leftarrow Y$. Artificial vertices

$$V_{-1} \equiv 2V_0 - V_1, \quad V_{m+1} \equiv 2V_m - V_{m-1} \tag{C 3}$$

| $i$ | $X_i$ (cm) | $Y_i$ (cm) |
|---|---|---|
| 0 | 0 | 0 |
| 1 | 9·225681 | −0·109890 |
| 2 | 31·011056 | 3·846153 |
| 3 | 40·140415 | 12·318963 |
| 4 | 45·675620 | 20·524091 |
| 5 | 48·524623 | 26·700479 |
| 6 | 53·408628 | 32·155536 |
| 7 | 71·438746 | 26·294730 |
| 8 | 88·980463 | 11·732882 |
| 9 | 107·890720 | 2·787639 |
| 10 | 141·578144 | 0·008453 |
| 11 | 150 | 0 |

TABLE 3

are defined so that the curve has zero curvature at the end points $V_0$ and $V_m$. The entire curve from $V_0$ to $V_m$ is of *class*-2, i.e. *the curve is continuous together with its first two derivatives* (so that slope $\theta$ and curvature $\kappa$, but not necessarily $d\kappa/dx$, are continuous). At a given abscissa $x$, to find the slope $\tan\theta \equiv d\zeta/d\xi$ and the curvature $k \equiv (d^2\zeta/d\xi^2)\cos^3\theta$, we solve

$$\xi(\lambda) - x = 0 \tag{C 4}$$

for $\lambda$ (using Newton–Raphson iteration) to find $\xi'$, $\zeta'$, $\xi''$ and $\zeta''$ (where a prime denotes $d/d\lambda$), so that

$$\frac{d\zeta}{d\xi} = \frac{\zeta'}{\xi'}, \quad \frac{d^2\zeta}{d\xi^2} = \frac{\zeta''}{(\xi')^2} - \frac{\xi''}{(\xi')^2}\frac{d\zeta}{d\xi}. \tag{C 5}$$

For the unsymmetric profile we take $m = 11$ and the vertices given in table 3.

## REFERENCES


BAUER, W. J. 1954 *Trans. A.S.C.E.* **119**, 1212–1233.

CHOW, V. T. 1959 *Open Channel Hydraulics*, pp. 370–380. McGraw-Hill.

DE BOOR, C. 1978 *A Practical Guide to Splines*, pp. 108–164. Springer.

DRESSLER, R. F. 1978 New nonlinear shallow-flow equations with curvature. *J. Hydraul. Res.* **16**, 205–220.

ESCOFFIER, F. F. 1958 *Trans. A.S.C.E.* **123**, 43–65.

HENDERSON, F. M. 1966 *Open Channel Flow*. Macmillan.

HENDERSON, F. M. & TIERNEY, D. C. 1963 Flow at the toe of a spillway, II – The "solid toe" spillway. *Houille Blanche* **1**, 42–50.

LOGANANTHARAJ, R. 1981 Generation of curves and surfaces. M.Eng. thesis, Division of Computer Applications, Asian Institute of Technology, Bangkok, Thailand.

SIVAKUMARAN, N. S. 1981 Shallow-flow over curved beds. D.Eng. thesis, Division of Water Resources Engineering, Asian Institute of Technology, Bangkok, Thailand.

SIVAKUMARAN, N. S., HOSKING, R. J. & TINGSANCHALI, T. 1981 Steady shallow flow over a spillway. *J. Fluid Mech.* **111**, 411–420.

STREETER, V. L. & WYLIE, E. B. 1975 *Fluid Mechanics*, pp. 471–473. McGraw-Hill, Kogakusha.